https://dx.doi.org/10.1016/j.envpol.2018.08.093

Mechanistic insights into adsorption and reduction of hexavalent chromium from water using magnetic biochar composites: Key roles of Fe_3O_4 and persistent free radicals

Delai Zhong[a], Yanrong Zhang[a], Linling Wang[a, *], Jing Chen[a], Yi Jiang[b], Daniel C.W. Tsang[b], Zezhou Zhao[a], Shupeng Ren[a], Zhenhua Liu[a], John C. Crittenden[c]

[a] *School of Environmental Science and Engineering, Huazhong University of Science and Technology, Wuhan, 430074, P.R. China*

[b] *Department of Civil and Environmental Engineering, The Hong Kong Polytechnic University, Hung Hom, Kowloon, Hong Kong, P.R. China*

[c] *Brook Byers Institute of Sustainable Systems and School of Civil and Environmental Engineering, Georgia Institute of Technology, Atlanta, GA 30332, United States*

* Corresponding author.

E-mail address: wanglinling@hust.edu.cn (L. Wang)

ABSTRACT

Magnetic biochar (MBC) has been used to remove hexavalent chromium (Cr(VI)) from water, but the roles of Fe_3O_4 and persistent free radicals (PFRs) in MBC in Cr(VI) removal are still less investigated. In this work, the MBC synthesized by microwave co-pyrolysis of solid-state $FeSO_4$ and rice husk was employed to remove Cr(VI) from water. In comparison to the rice husk biochar (BC), the MBC exhibits the 3.2- and 11.7-fold higher adsorption and reduction efficiency of Cr(VI), resulting in the higher Cr(VI) removal efficiency (84.3%) and equilibrium adsorption capacity of MBC (8.35 mg g^{-1}) than that (26.5% and 2.63 mg g^{-1}) of BC. Multiple characterization results revealed that the high Cr(VI) removal performance of MBC was mainly attributed to the presence of active Fe_3O_4 and carbon-centered PFRs in the porous and graphitic MBC. The Fe_3O_4 not only provided active chemisorption/reduction sites for Cr(VI) via its $Fe(II)_{oct}$ and $Fe(III)_{oct}$ coordination, but also facilitated the generation of more active electron donating carbon-centered PFRs than carbon-centered PFRs with an oxygen atom in the graphitic structure to reduce Cr(VI). The presence of Fe_3O_4 also elevated 36.7 m^2 g^{-1} of BET-surface area and 0.043 cm^2 g^{-1} of pore volume of MBC, promoting the Cr(VI) removal. The Fe_3O_4 and carbon-centered PFRs contributed to ~81.8% and ~18.2% of total Cr(III) generation, respectively. In addition, the initial solution pH was responsible for determining the relative significance of Cr(VI) adsorption and reduction. This study provides new insights into the mechanisms of Cr(VI) removal from water by the MBC.

Capsule: This study shed new mechanistic light on the key roles of Fe_3O_4 and persistent free radicals in the MBC in the removal of Cr(VI).

Keywords:

Magnetic biochar; Hexavalent chromium; Synergistic removal; Magnetite; Persistent free radicals.

1. Introduction

Hexavalent chromium (Cr(VI)) in water poses severe threat to human health and environment due to its high toxicity, carcinogenicity, and mutagenicity (Qian et al., 2017). It has been designated as a priority pollutant by the U.S. EPA (Guo et al., 2012). Various Cr(VI) treatment technologies have been reported, such as adsorption (Zhou et al., 2018), electrocoagulation (Pan et al., 2016), membrane separation (Duan et al., 2017), and ion exchange (Rapti et al., 2016). Among all these strategies, adsorption is one of the most effective methods owing to its high efficiency and cost effectiveness (Liu et al., 2016). In comparison to Cr(VI), trivalent chromium (Cr(III)) is almost 100 times less toxic, less soluble, less mobile, and can readily form precipitate (e.g., $Cr(OH)_3$) in aqueous solutions (Katz Sidney and Salem, 1993; Zhang et al., 2017a). Hence, the effective strategy for concurrent Cr(VI) reduction and in situ adsorption arouses extensive interest for detoxification of Cr(VI)-contaminated media (Jiang et al., 2014; Wang et al., 2015). It minimizes the associated health and ecological risks through the decrease of total chromium (Cr(tot)) in water.

Magnetic biochar (MBC) through the introduction of Fe_3O_4 has been applied in the treatment of Cr(VI) contaminated water owing to its easy separation property and high removal capacity (Cao et al., 2016; Qiu et al., 2015). For example, Wang et al. (2014) reported that MBC exhibits an excellent magnetic separation property for Cr(VI)-containing electroplating wastewater, and the turbidity of adsorption-treated solution

could be significantly reduced after 10 min magnetic separation. Recently, several studies showed that MBC has a higher Cr(VI) removal capacity than unmodified biochar (Li et al., 2013; Qiu et al., 2014; Qiu et al., 2015). They further suggested that the proposed mechanisms involve reduction of Cr(VI) to Cr(III) by functional groups (i.e., C–O, and C–C) of biochar and chemical adsorption on Fe_3O_4 in MBC. However, the relative significance of the reduction and sorption roles of Fe_3O_4 and other potentially active components in MBC in the removal of Cr(VI) is still unclear.

Recently, an unintentional product (i.e., solid-phase free radicals (SFRs)) after biomass pyrolysis, although ubiquitous in biochar, has been found by using electron paramagnetic resonance technique (Chu et al., 2017; Fang et al., 2015b; Yang et al., 2017). Compared to commonly studied free radicals (e.g., •OH), these SFRs exhibit reactivity with longer time, ranging from days to months, and thereby are referred as persistent free radicals (PFRs) (Yang et al., 2017). The PFRs have been reported to mediate electron-transfer reactions and alter the transformation of contaminants in water (Fang et al., 2014; Yang et al., 2016). In particular, PFRs in biochar have been demonstrated to donate electrons to oxidizing agents, including persulfate, hydrogen peroxide, and molecular oxygen, to form reactive oxygen species for the degradation of organic pollutants (Fang et al., 2015a; Fang et al., 2015b; Yang et al., 2017). However, the role of PFRs in the MBC in treatment of Cr(VI)-contaminated water remains relatively nascent.

In the present study, MBC prepared by microwave (MW) pyrolysis of rice husk mixed

with ferrous sulfate ($FeSO_4$) were employed for Cr(VI) removal. The main objective of this research was to decipher the roles of Fe_3O_4 and PFRs in the MBC in the Cr(VI) removal process and underlying mechanisms of Cr(VI) removal. Detailed comparisons for Cr(VI) removal performances by MBC and BC, especially adsorption and reduction capacity, were performed. In particular, X-ray photoelectron spectroscopy (XPS), electron paramagnetic resonance (EPR), Raman spectroscopy, electrochemical impedance spectroscopy (EIS) were used to reveal the roles of Fe_3O_4 and PFRs in the MBC in the Cr(VI) removal process. Knowledge of this study could shed new mechanistic light on the Cr(VI) removal by MBC.

2. Materials and methods

2.1. Chemicals

All the chemicals used in this study are described in the Text S1 of Supporting information (SI).

2.2. Magnetic biochar preparation and characterization

Rice husk (RH) was collected from a farm located in Hubei province, China. The collected RH was washed with deionized water (18.2 MΩ cm), and air-dried at room temperature. A 25-g portion of RH was evenly mixed with 2.5 g of solid $FeSO_4$ powder, then the mixture was manually milled. The milled solid particles (with the particle size ≤

103 0.149 mm) was subsequently transferred into a silicon carbide (which is an excellent MW
104 absorber) vessel covered with a cap in a MW oven (Boyou Microwave Technology
105 Development Co., Ltd., Nanjing, China) for co-pyrolysis (1 kW, 30 min) under oxygen-
106 limited conditions. The obtained biochars were simply pretreated by 0.1 M HCl solution
107 for ~5 min to remove some possible impurities (e.g., $FeSO_4$, and alkali-metal salts) in the
108 MBC, followed by deionized water washing until the pHs reached stable (~4.5). After
109 being washed, these solid particles were dried in a vacuum oven, then passed through a
110 0.149-mm sieve again, and finally stored in amber vials (4 °C) for later use. For
111 comparison, the unmodified biochar was prepared without $FeSO_4$ powder by the similar
112 procedure. These two biochars aforementioned were labelled as MBC and BC,
113 respectively. Details of the preparation processes are described in Text S2 of SI. The
114 production yield of MBC was 33.5%, lower than that (47.2%) of BC.

115 Fe speciation (i.e., Fe^{2+} and Fe^{3+}) and content of biochar samples after 1.0 M HCl
116 digestion for 24 h were analyzed with a modified method (Liao et al., 2017) (Text S3 of
117 SI). Meanwhile, the other transition metals (e.g., Cu and Mn) in the digestion solution
118 were also determined by the inductively coupled plasma optical emission spectrometry
119 (ICP–OES, Optima 8300, PerkinElmer, U.S.) because they might influence the Cr(VI)
120 reduction (Table S1). The characterizations of morphology, element contents (C, N, O,
121 and H), textural properties, crystalline structure, surface chemistry, Zeta potentials, PFRs
122 species and contents, and electrochemical properties are presented in detail in Text S4 of

SI.

2.3. Batch experiments

Unless otherwise specified, the batch experiment was conducted as follows: 0.2 g of adsorbent (10 g L^{-1}) was added to 20 mL of 100 mg L^{-1} Cr(VI) solution in a 50 mL plastic centrifuge tube with screw cap. The initial pH solution was adjusted to 3.0 ± 0.1 with 0.01 and 0.1 M HNO_3 or NaOH solution. The HNO_3 was selectively used to adjust the initial solution pH due to little effect of HNO_3 itself on Cr(VI) reduction (Text S5 of SI). Then the mixture was incubated at a rate of 200 rpm at 25 °C for 1440 min (24 h). The preliminary test demonstrated that the Cr(VI) removal had reached equilibrium within 1440 min (Fig. S1). At different time intervals, 2 mL of sample solutions were sampled and then filtered through a 0.45 μm membrane for the subsequent analysis. The Cr(VI) and Cr(tot) in the filtrate were measured by a 1,5-diphenylcarbazide method and ICP–OES, respectively. The aqueous Cr(III) concentration was calculated based on the difference of Cr(tot) and Cr(VI). Meanwhile, the Fe(II), Fe(III), and Fe(tot) concentrations were also analyzed, respectively (Liao et al., 2017). The resulting solid residues were freeze-dried and then analyzed.

The effect of initial solution pH (from 1.0 to 11.0) was investigated. The effect of anion species (2 mmol L^{-1} of Cl^-, NO_3^-, and SO_4^{2-}, respectively) on the adsorption and reduction of Cr(VI) was also tested. All the experiments data were the average values of

143 triplicate determinations, with the relative errors below 5%.

144

145 **3. Results and discussion**

146 *3.1. Characterization*

147 As shown in Fig. S2a and S2b, the MBC exhibited more honeycomb and tunnel-like
148 structures than that of BC. Small pores (0.5–1 μm) were well distributed in the inner-wall
149 of MBC. This was possibly because the MW "hotspot" effect in the presence of iron-
150 based MW absorbers could promote the release of low-molecular-weight organic matter
151 of rice husk, resulting in the development of porous structure as well as BET-surface area.
152 As expected, the BET-surface area and pore volume of MBC were nearly doubled
153 compared to that of BC (76.9 vs. 40.2 $m^2 g^{-1}$, and 0.087 vs. 0.044 $cm^3 g^{-1}$, respectively),
154 which suggested that the $FeSO_4$ addition could improve the textural properties of MBC.
155 The texture properties of as-synthesized MBC were superior to that (BET-surface area of
156 1.04–50.0 $m^2 g^{-1}$) of many magnetic adsorbents reported in previous studies (Cui et al.,
157 2015; Mohan et al., 2014; Rajput et al., 2016; Ren et al., 2013). In the aid of the EDS
158 spectrum (inset in Fig. S2b), we observed that iron oxide was anchored into the tunnel-
159 like structures of MBC. It was reported that the attachment of iron oxide could improve
160 interface contact and mitigate acid dissolution, thereby facilitating the electron transfer
161 and acid-stability of the composite (Veerakumar et al., 2016). TEM characterization
162 further validated the presence of mosaic of iron oxide in the thin MBC layer (Fig. S2c).

High-resolution TEM (HRTEM) analysis demonstrated that the iron oxide exhibited a well crystalline texture, and its lattice space was 0.294 nm, which might be corresponding to (220) plane of Fe_3O_4 (Fig. S2d).

To verify the presence of magnetite Fe_3O_4 in the MBC, XRD analysis was employed to check the crystalline structure of MBC as well as BC. As shown in Fig. S2e, after the $FeSO_4$ addition, the new diffraction peaks at $2\theta = 30.1^{\circ}$, 35.4°, 43.2°, 56.9°, and 62.5° were observed on the MBC, which could be ascribed to respective facets of the (220), (311), (400), (511), and (440) planes of magnetite Fe_3O_4 (PDF card 19-0629) (Li et al., 2013), which was consistent with the XRD pattern of standard Fe_3O_4. The digestion test showed that the contents of Fe(II) and Fe(III) in the MBC were 0.272 and 0.493 mmol g^{-1} (i.e., Fe(II)/Fe(III) = 1/1.8), respectively, which was fairly close to the expected ratio of 1/2 (Fe_3O_4). This suggested the presence of Fe_3O_4 with the average content of 0.255 mmol g^{-1} in the MBC. The Fe_3O_4 formation in the MBC could be explained by the reactions R1–R4. During the MW heating process, $FeSO_4 \cdot 7H_2O$ was first subjected to dehydration reaction (R1), then the formed $FeSO_4$ was further decomposed into Fe_2O_3 by the reaction R2 (Fig. S3), as reported in previous literature (Kanari et al., 2016). After that, Fe_2O_3 was finally reduced to Fe_3O_4 by the main intermediates CO (R3) and H_2 (R4) produced from biomass pyrolysis (Yao et al., 2016).

$$FeSO_4 \cdot 7H_2O \xrightarrow{MW} FeSO_4 + 7H_2O \quad (R1)$$

$$FeSO_4 \xrightarrow{MW} Fe_2O_3 + SO_2 + O_2 \quad (R2)$$

$$Fe_2O_3 + CO \xrightarrow{MW} Fe_3O_4 + CO_2 \quad (R3)$$

$$Fe_2O_3 + H_2 \xrightarrow{MW} Fe_3O_4 + H_2O \quad (R4)$$

The FTIR spectra of MBC and BC are presented in Fig. S2f. In comparison to the BC, the MBC exhibited a new peak at ~586 cm^{-1}, which was indicative of stretching vibration of Fe–O in Fe_3O_4. The peak positions of aromatic C=O and C–O vibrations considerably shifted from 1585 and 1095 cm^{-1} to 1541 and 1121 cm^{-1}, respectively, suggesting that these two groups were likely to interact with Fe_3O_4 (Jiang et al., 2014; Jin et al., 2015; Rao et al., 2013). Their relative peak intensities also decreased, which may be attributed to decomposition at a high pyrolysis temperature due to the presence of iron-based MW absorbers. The magnetic property of MBC was investigated. Fig. S4 shows that the MBC was well dispersed in Cr(VI) containing solution, the spent MBC could be easily separated from the dispersion solution by holding the samples close to a magnet. This indicated that the magnetic separation of MBC was feasible for the treatment of Cr(VI)-contaminated water by an external magnetic field.

3.2. Cr(VI) adsorption and reduction performance

The MBC and BC were employed to remove Cr(VI) from water. The time profiles of aqueous Cr species variations with MBC and BC show contrasting differences (Fig. 1a and 1b). For the BC-Cr(VI) system, the aqueous Cr(VI) concentration slowly decreased from 100 to 73.6 mg L^{-1} within 1440 min, whereas the aqueous Cr(III) concentration was

extremely low (< 0.5 mg L^{-1}), reflecting that the BC had a comparatively poor Cr(VI) removal performance. In contrast, the Cr(VI) removal by the MBC clearly presented three stages in the whole process (0−1440 min). More information about the subdivision of three stages can be seen in the Text S6 of SI. The aqueous Cr(VI) concentration dramatically decreased from 100 to 33.2 mg L^{-1} (0−160 min), gradually decreased to 15.8 mg L^{-1} (160–1120 min), and ultimately equilibrated to 15.7 mg L^{-1} (1120–1440 min). This was mainly ascribed to the electrostatic attraction between the Cr(VI) anions (e.g., $HCrO_4^-$) and the positive surface charge of MBC (pH_{zpc} = 4.4, solution pH 3.0–4.4) (Fig. S5 and S6). At the respective stage, the aqueous Cr(III) generated by Cr(VI) reduction clearly increased from 0 to 5.1 mg L^{-1}, slowly reduced to 0.9 mg L^{-1}, and finally achieved 0.8 mg L^{-1}. This indicated that some of positively charged Cr(III) (Fig. S7) was initially released into solution from solid MBC due to the electrostatic repulsion (solution pH 3.0–4.4), then adsorbed onto MBC via electrostatic attraction again (solution pH 4.4–5.4). These results revealed that MBC had a much higher removal efficiency (84.3%) than BC (26.5%), also confirmed that the Cr(VI) removal by MBC and BC was a hybrid adsorption-reduction process.

To decipher the difference of Cr(VI) removal between MBC and BC, the abilities of MBC, BC and pure Fe_3O_4 to adsorb Cr(VI) (η_{ads}) were first evaluated using Eq. (1).

$$\eta_{ads}\ (\%) = \frac{(C_0 - C_t^T)}{C_0} \times 100 \qquad (1)$$

where C_0 is the aqueous Cr(VI) concentration at the time 0 (min). C_t^T (mg L^{-1}) is the

223 aqueous Cr(tot) concentrations (mg L^{-1}) at the time t (min).

224 As presented in Fig. 1c, the Cr(VI) adsorption efficiency of BC was 26.3%, which was
225 3.2-fold lower than that (83.5%) of MBC. In contrast, pure Fe_3O_4 (at an amount
226 equivalent to Fe_3O_4 content of MBC addition) had just 31.2% of Cr(VI) adsorption
227 efficiency, which was substantially lower than that of MBC. Moreover, the sum of Cr(VI)
228 adsorption efficiency of their individuals was 57.5%, which was less than that of MBC.
229 This demonstrated that the presence of Fe_3O_4 in the MBC played a synergistic role in the
230 Cr(VI) adsorption process. The equilibrium Cr(VI) adsorption capacities of MBC, BC,
231 and Fe_3O_4 were 8.35, 2.63, and 3.12 mg g^{-1}, respectively. The adsorption capacity
232 normalized with BET-surface area were also calculated (Table S2), which reflected that
233 the higher Cr(VI) adsorption capacity of MBC was not ascribed only to the BET-surface
234 area, but probably involved the Cr(VI) reduction.

235 Based on the Cr $2p_{3/2}$ XPS quantitative analyses of Cr-loaded adsorbents and aqueous
236 Cr(III) concentration after 1440 min (Table S3 and Fig. 2a), we further investigated the
237 Cr(VI) reduction efficiencies (η_{red}) of MBC, BC, and pure Fe_3O_4 by employing Eq. (2),
238 respectively.

239 $$\eta_{red}\ (\%) = \frac{(C_t^T - C_t) + (C_0 - C_t^T)\, R_s}{C_0} \times 100 \qquad (2)$$

240 where C_t is the aqueous Cr(VI) concentrations (mg L^{-1}) at the time t (min). R_s (%) is the
241 percent of Cr(III) to Cr(tot) adsorbed on the surface of adsorbents.

242 As depicted in Fig. 1d, we found that ~58.7% of Cr(VI) was reduced by MBC, while

the Cr(VI) reduction efficiency of BC and pure Fe_3O_4 was just ~5.0% and ~27.4% (more information can be seen in Text S7), respectively. This indicated that the MBC had the most reduction sites for Cr(VI). Furthermore, ~46.9% of Cr(VI) reduction resulted from the full oxidation of Fe_3O_4 in the MBC (Fig. 2b), higher than that (27.4%) of pure Fe_3O_4, which might be due to well-dispersion of Fe_3O_4 in the MBC. The active carbon-based compartment of MBC contributed to ~11.8% of Cr(VI) reduction, higher than that (~5.0%) of BC. This revealed that the carbon-based compartment of MBC had a higher reduction capacity than that of BC, which might be related to different types and/or contents of reduced components in the adsorbents. After the Cr(VI) removal, the solution pH increased from 3.0 to 5.4 for MBC, 5.7 for BC, and 4.2 for Fe_3O_4, i.e., the apparent pH change of MBC-Cr(VI), BC-Cr(VI), and Fe_3O_4-Cr(VI) solution was 2.4, 2.7, and 1.2, respectively. However, the apparent pH change unnecessarily indicated the Cr(VI) reduction efficiency due to the inherent alkaline properties of carbon-based adsorbents. In summary, the formation of Fe_3O_4 in the MBC could induce a synergistic effect on the generation of adsorption and reduction sites for Cr(VI) instead of a simple sum of their individuals, accounting for the significant improvement of Cr(VI) removal.

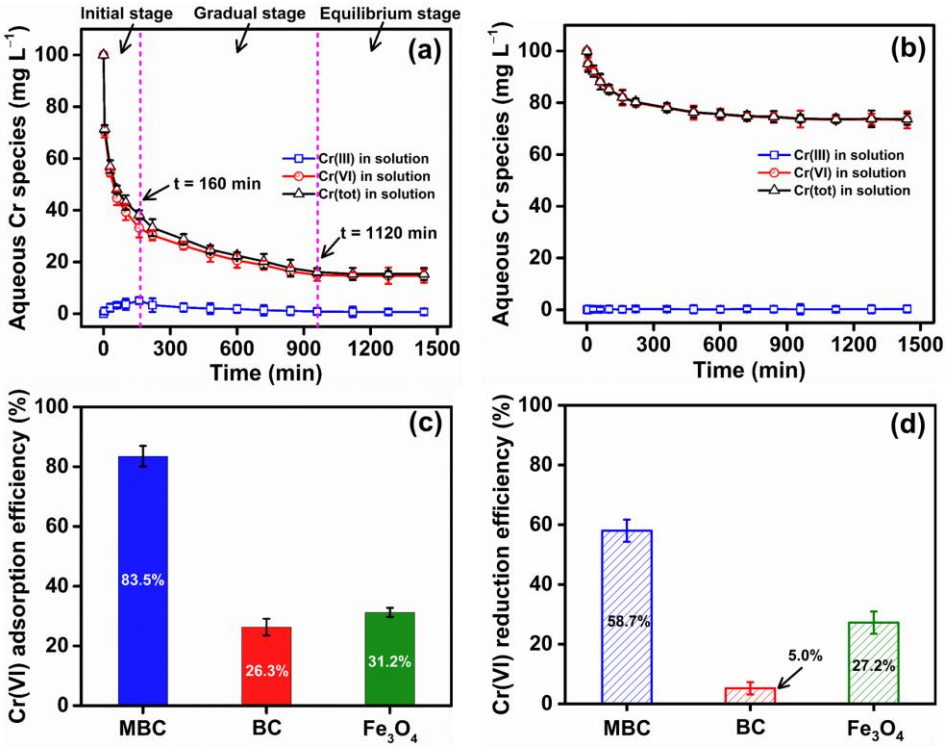

Fig. 1. Time profiles of aqueous Cr species variation with MBC (a) and BC (b), comparisons of Cr(VI) adsorption (c) and reduction (d) efficiency of MBC, BC, and pure Fe_3O_4. Conditions: 10 g L^{-1} of MBC and BC, 0.6 g L^{-1} of pure Fe_3O_4 (at an amount equivalent to Fe_3O_4 content of MBC addition); the initial solution pH of 3.0; the initial Cr(VI) concentration of 100 mg L^{-1}; reaction time of 0−1440 min; reaction temperature of 25 ˚C.

3.3. Roles of Fe_3O_4 and PFRs in Cr(VI) adsorption and reduction

3.3.1. Role of Fe_3O_4

The surface information of MBC before and after the Cr(VI) removal was checked to propose the role of Fe_3O_4 in the adsorption and reduction of Cr(VI). As presented in the

Fe $2p_{3/2}$ XPS spectra in Fig. 2b and Table S4, before the Cr(VI) removal, three peaks at 710.6, 711.6, and 714.1 eV were observed on the MBC, which were attributed to Fe(II) and Fe(III) in octahedral coordination ($Fe(II)_{oct}$ and $Fe(III)_{oct}$) and Fe(III) in tetrahedral coordination ($Fe(III)_{tet}$) of Fe_3O_4, respectively (Bhargava et al., 2007; Eltouny and Ariya, 2012; Wilson and Langell, 2014; Yamashita and Hayes, 2008). After the Cr(VI) removal, the $Fe(II)_{oct}$ peak obviously disappeared, while a new peak emerged at 719.9 eV for Fe $2p_{3/2}$ satellite peak, indicating that Fe(II) was oxidized to Fe(III). The XRD pattern of Cr-loaded MBC (Fig. S8a) should be attributed to the presence of γ-Fe_2O_3 rather than Fe_3O_4, although they have exhibited similar XRD patterns. This assignment can be further consolidated by the XPS results that demonstrated a fully oxidized state of iron oxides and previous studies (Liu et al., 2012; Pinakidou et al., 2016; Yuan et al., 2010). During the oxidation process of the $Fe(II)_{oct}$ atoms to Fe(III), cation vacancies were generated at the octahedral sites. Considering the balance of electroneutrality, there should be either the electron migration or diffusion of Fe(II) from internal Fe_3O_4 to the oxidized iron-based surface of bulk MBC. Therefore, the adsorbed Cr(VI) could be reduced to Cr(III) by reaction with the migrated electrons or Fe(II) (Liu et al., 2015). In addition, the variation of $Fe(III)_{oct}$ peak suggested the participation of $Fe(III)_{oct}$ in the Cr(VI) adsorption. These results demonstrated that the $Fe(II)_{oct}$ and $Fe(III)_{oct}$ coordination in Fe_3O_4 could provide the active chemisorption/reduction sites for Cr(VI) via the reactions R5–R6, promoting the Cr(VI) removal. Such active chemisorption/reduction sites for

Cr(VI) was not affected by competitive anions, such as Cl^-, NO_3^-, and SO_4^{2-} in our supplementary tests (Fig. S9).

$$\equiv Fe(II)_{oct} + Cr(VI)_{ads} + H^+_{ads} \rightarrow \equiv Fe(III)_{oct}–Cr(III) + H_2O \quad (R5)$$

$$\equiv Fe(III)_{oct} + Cr(VI)_{ads} \rightarrow \equiv Fe(III)_{oct}–Cr(VI) \quad (R6)$$

As provided in Table S4, the Fe(II)/Fe(III) ratio of MBC decreased from 0.5 to 0 after the Cr(VI) removal, indicating that Fe_3O_4 was completely oxidized to Fe_2O_3. Thus, 0.051 mmol Fe_3O_4 in 0.2 g of MBC resulted in 0.018 mmol of Cr(III) generation, accounting for ~81.8% (i.e., 0.018 mmol/0.022 mmol) of the sum of Cr(III) (i.e., 0.032 mmol × ~69.6%) on the surface of MBC. In other words, the complete oxidation of Fe_3O_4 quantitatively contributed to the ~81.8% of total Cr(III) generation on the surface of MBC particles.

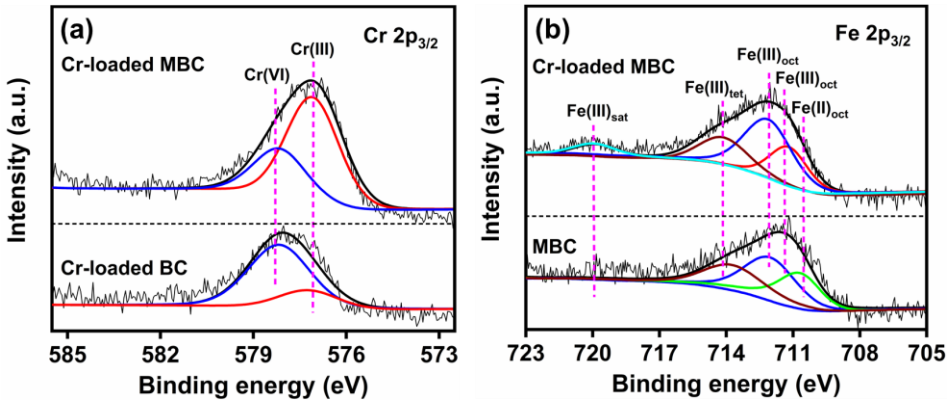

Fig. 2. (a) Cr $2p_{3/2}$ and (b) Fe $2p_{3/2}$ XPS spectra of MBC or BC before and/or after the Cr(VI) removal.

3.3.2. Role of PFRs

We hypothesized that the Cr(VI) reduction capacities of MBC and BC might be related to PFRs, and therefore analyzed the EPR spectra to quantify PFRs in the MBC and BC. Both MBC and BC had the broad singlet EPR signals, which indicated the presence of PFRs in both biochars (Fig. 3a). The PFRs concentration of MBC was 5.754×10^{17} spins g^{-1}, lower than that (8.943×10^{17} spins g^{-1}) of BC, reflecting the MBC contained less PFRs. It was reported that g-factors of PFRs are less than 2.0030 for carbon-centered radicals but fall in the range of 2.0030–2.0040 for carbon-centered radicals with an adjacent oxygen atom, respectively, whereas g-factors are over 2.0040 for oxygen-centered radicals (Yang et al., 2017). Based on our results, g-factors of MBC and BC were 2.0026 and 2.0038, which were characteristic of carbon-centered radicals (denoted as aromatic •C) and carbon-centered PFRs with an adjacent oxygen atom (denoted as •C–O), respectively. After the Cr(VI) removal, we found that these PFRs concentrations of MBC (1.491×10^{17} spins g^{-1}) and BC (1.108×10^{17} spins g^{-1}) were consumed to different extents (Fig. 3b). This suggested that these two PFRs could participate in the Cr(VI) reduction by the reaction R7, but the aromatic •C in the MBC showed a higher reduction capacity than that of •C–O in the BC.

$$\equiv\text{PFRs} + \text{Cr(VI)}_{ads} + \text{H}^{+}_{ads} \rightarrow \equiv\text{Oxidized organic matter} + \text{Cr(III)}_{ads} + \text{H}_2\text{O} \qquad \text{(R7)}$$

These could be ascribed to the following reasons: (1) the carbon atom in aromatic •C (0.007 *e*) had a lower positive Mulliken charge than that in •C–O (0.150 *e*) (calculated with Material Studio version 8.0) (Li et al., 2017), indicating that the former had a higher

electron donating ability to reduce Cr(VI) (Fig. S10). The detailed calculation process can be seen in the Text S8 of SI; (2) the carbon-based compartment of MBC with graphitic structure possessed a higher electrical conductivity compared to BC, suggesting that MBC could promote the transfer of electrons from the reduced components such as PFRs and Fe_3O_4 to Cr(VI).

To verify this, Raman spectroscopy was used to investigate the graphitic properties of MBC and BC that may affect the ability of electron transfer. The characteristic D band is owing to the disorder in aromatic ring structure in sp^3carbon atoms, and G band is related to the vibration of carbon atoms in sp^2 sites (Luo et al., 2014; Zhang et al., 2016). The intensity ratio of the D and G band (I_D/I_G) is a useful indicator to evaluate the ordered and disordered crystal structures of carbon (Li et al., 2013). Fig. 3c demonstrates that the D and G bands for the BC and MBC at about 1353 cm^{-1} and 1590 cm^{-1} were both observed, respectively, which were in good correspondence with the literature (Zhang et al., 2016). The I_D/I_G ratio of MBC was 0.78, lower than that (0.93) of BC, which indicated the presence of more sp^2 graphitic domains in the MBC. This suggested that MBC could facilitate a larger extent of electron transfer reactions to improve the Cr(VI) reduction. This was because the MW "hotspot" effect could enhance localized pyrolysis temperature to facilitate the development of graphitic structure in the presence of iron-based MW absorbers (e.g., Fe_3O_4 and Fe_2O_3) during the MW irradiation process (Sun et al., 2011; Wang et al., 2014).

EIS tests were further performed and presented in Fig. 3d, in which the smaller radius of semicircle for MBC than that for BC revealed an increase in electrical conductivity in the MBC due to the formation of graphitic structure. In addition, as summarized in Table S5, the H/C and O/C ratios of MBC were lower than those of BC (0.02 vs. 0.05, and 0.93 vs. 1.17, respectively), suggesting that the MBC had a higher potential to induce electron transfer reactions than that of BC (Sun et al., 2017). Therefore, the formation of aromatic •C in the graphitic carbon-based compartment of MBC could play an important role in the Cr(VI) reduction. Nevertheless, considerable amounts of PFRs still remained in the MBC after the Cr(VI) removal, which was possibly because the low concentrations of Cr(VI) (~15.7 mg L^{-1}) and proton ($1.0 \times 10^{-5.4}$ M) at the final stage (Fig. 1a and Fig. S6) could not initiate the redox reaction. This also implied that the reactivity of Fe_3O_4 was higher for Cr(VI) reduction than that of PFRs.

Although the carbon-containing groups (e.g., C–C) were suggested to reduce Cr(VI) (Qiu et al., 2015), as shown in Fig. S11, the contents of carbon-containing (i.e., C–C, C=C, and C–H) groups displayed little differences (Table S6) before and after the Cr(VI) removal. Therefore, it is important to note that these functional groups should have a minimal role in the Cr(VI) reduction due to a lower reactivity compared to that of active Fe_3O_4 and PFRs. Owing to the pH- and concentration-dependent Cr(VI) redox potential (Eh), the increasing pH (from 3.0 to 5.4) and decreasing Cr(VI) concentration (from 100 to 15.7 mg L^{-1}) during the Cr(VI) removal process possibly inhibited the redox reactions

between these functional groups and Cr(VI), especially in the presence of active Fe_3O_4 and PFRs. After the Cr(VI) removal, the slight shifts of C–O and C=O groups suggested the complexation with Cr(III) (Fig. S8b), which was consolidated by previous studies (Zhang et al., 2017b; Zhao et al., 2016). Also the peak position shifted from 586 to 578 cm^{-1} demonstrated the presence of Fe–O–Cr bond (Rajput et al., 2016), which may indicate the formation of some precipitates (e.g., $Fe_xCr_{1-x}(OH)_3$). In addition, the effects of inherent components such as dissolved organic matter (DOM) and transition metals (Fe, Mn, and Cu) on the Cr(VI) reduction were explored, which had little effect on the reduction of Cr(VI) (Text S9). It appears that Cr(VI) could not be reduced by the traditional functional groups, DOM, and transition metals in the MBC, hence the aromatic •C in the MBC was considered to be responsible for the production of the rest of 0.004 mmol Cr(III), accounting for 18.2% of the total Cr(III) generation (i.e., 0.004 mmol/0.022 mmol).

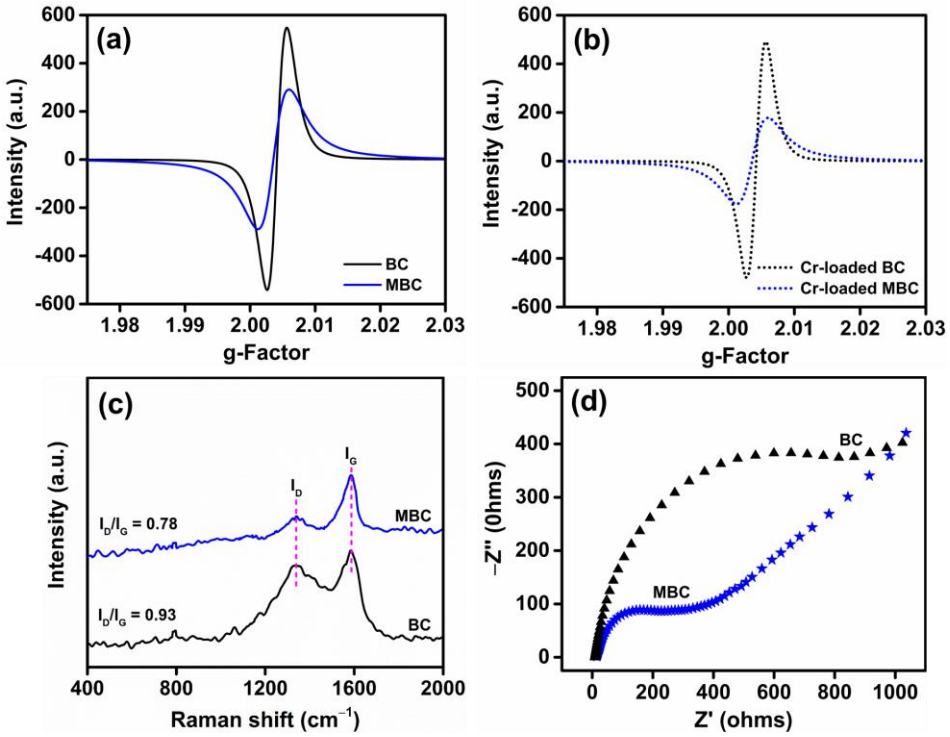

Fig. 3. EPR spectra of BC (a) and MBC (b) before and after the Cr(VI) removal, Raman spectra (c), and EIS (d) of BC and MBC.

3.4. Effect of solution pH

The aqueous Cr(VI) concentration was found to dramatically increase from 0.2 to 70.3 mg L^{-1} as the initial solution pH increased from 1.0 to 11.0 (Fig. 4). There was a strong and positive correlation (R^2 = 0.997) between the initial solution pH and residual Cr(VI) concentration (Fig. S12). The results demonstrated that the low initial solution pH could facilitate the Cr(VI) removal. Fig. S13 shows the major speciation of Cr(VI) in aqueous solution were $HCrO_4^-$ CrO_4^{2-}, and $Cr_2O_7^{2-}$, whose distributions were highly dependent on solution pH at a given total chromate concentration (100 mg L^{-1}). At solution pH 1.0–6.3, the predominant $HCrO_4^-$ in the aqueous solution had more negative adsorption free

393 energy than that of other two Cr(VI) anions (i.e., CrO_4^{2-} and $Cr_2O_7^{2-}$) (Rajput et al., 2016),
394 thus improving the Cr(VI) adsorption. However, CrO_4^{2-} was dominant above pH 6.3,
395 which was unfavorable for the Cr(VI) adsorption. In addition, a lower pH value can
396 facilitate Cr(VI) reduction to Cr(III) by MBC (Table S7 and Fig. S14), thereby resulting
397 in the higher Cr(VI) removal.

398 The initial solution pH also had a significant effect on the surface charge and solubility
399 of MBC. The high Cr(VI) removal by electrostatic attraction occurred below solution pH
400 4.4 (pH_{zpc} = 4.4) where the surface of MBC had a net positive charge (e.g., $FeOH_2^+$ in
401 Fe_3O_4 and $–COOH_2^+$ in functional groups). However, the surface charge of MBC became
402 more negative (e.g., $Fe–O^-$ and $–COO^-$) with increasing pH from 4.4 to 11.0. This
403 indicated that both stronger electrostatic repulsion and higher competition with OH^-
404 hindered the Cr(VI) removal. Moreover, Fe_3O_4 was reported to be ineffective for the
405 Cr(VI) adsorption and reduction under basic conditions (He and Traina, 2005), and
406 solution pH was expected to affect Fe dissolution from iron-based composites. Hence, the
407 concentrations of Fe(II) and Fe(III) in solution were simultaneously monitored at pH 1.0–
408 11.0 (Fig. S15). At pH 1.0, only Fe(III) (113.3 mg L^{-1}) instead of Fe(II) was detected in
409 the solution. This suggested that the dissolved Fe(II) from the MBC was fully oxidized to
410 Fe(III) by Cr(VI) in the solution, i.e., homogeneous redox reaction. At pH ≥ 3.0, both
411 Fe(II) and Fe(III) concentrations in the solution were undetectable, reflecting that the
412 MBC was relatively stable under acidic condition and the Cr(VI) removal was a

heterogeneous redox process.

In addition, the effect of solution pH on PFRs for the Cr(VI) reduction was investigated. As seen in Fig. S16, after the Cr(VI) removal, the decreasing intensity of EPR signals was clearly observed with decreasing solution pH, consistent with the residual Cr(VI) concentration in the solution. This implied that the higher oxidation potential of Cr(VI) at lower pH could stimulate its reduction by PFRs. At a concentration equivalent (mg L^{-1}), the higher concentration of Cr(III) generation (more than 73.8 mg L^{-1}) at pH 1.0 than that at pH 3.0 (58.7 mg L^{-1}) further supported that more Cr(VI) could be reduced by PFRs at a lower pH. These confirmed the high dependence of reduction of Cr(VI) by PFRs on the solution pH.

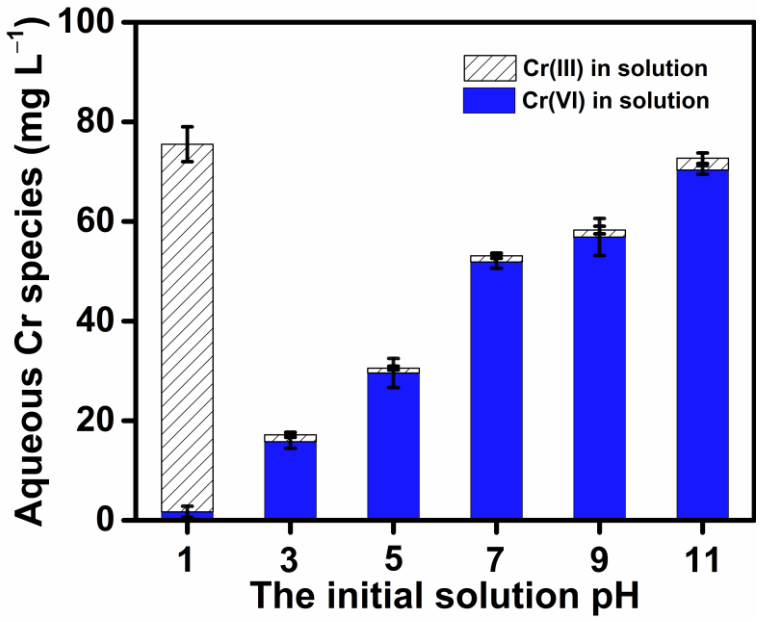

Fig. 4. Effect of initial solution pH on the Cr(VI) adsorption and reduction. Conditions: 10 g L^{-1} of MBC; the initial solution pH of 1.0–11.0; the initial Cr(VI) concentration of 100 mg L^{-1}; reaction time of 1440 min; reaction temperature of 25 ˚C.

3.5. Mechanisms of the Cr(VI) removal by the MBC

Based on the aforementioned results and analyses, the mechanisms of Cr(VI) removal by Fe_3O_4 and carbon-centered PFRs in the MBC at the initial solution pH 3.0 were proposed and illustrated in Scheme 1: (1) The Cr(VI) was electrostatically adsorbed onto the $Fe(II)_{oct}$ and $Fe(III)_{oct}$ coordination in Fe_3O_4. The adsorbed Cr(VI) could be partially reduced to Cr(III) by the $Fe(II)_{oct}$ coordination to form precipitates (e.g., $Fe_xCr_{1-x}(OH)_3$) as well as small release of Cr(III) cation due to electrostatic repulsion, while the rest of Cr(VI) interacted with the $Fe(III)_{oct}$ coordination via lattice oxygen. At the final stage, some of released Cr(III) could be again adsorbed onto the MBC by the electrostatic adsorption. (2) The Cr(VI) could be brought into close proximity with carbon-based compartment of MBC, subsequently reduced by adjacent carbon-centered PFRs as well as far carbon-centered PFRs in the graphitic basal MBC via electron conduction. Finally, the formed Cr(III) can complex with the functional groups (e.g., C–O and C=O) on the surface of MBC.

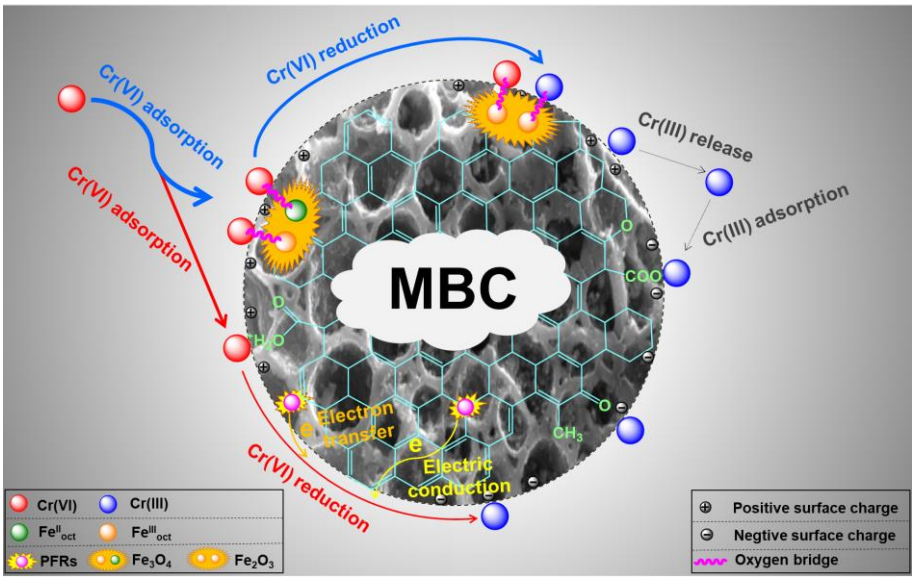

442

443 **Scheme 1.** Mechanisms of the Cr(VI) removal from solution by the MBC.

444

445 **4. Conclusions**

446 In this work, we prepared the MBC with active Fe_3O_4 and carbon-centered PFRs using
447 one-step microwave co-pyrolysis of rice husk and solid $FeSO_4$, then systematically
448 investigated the Cr(VI) removal behaviors and deciphered the key roles of these two
449 active components in the Cr(VI) removal from water. The MBC exhibited 84.3% of Cr(VI)
450 removal efficiency, which was a much higher than BC (26.5%). The $Fe(II)_{oct}$ and $Fe(III)_{oct}$
451 coordination in Fe_3O_4 can act as active chemisorption/reduction sites to directly remove
452 Cr(VI). Interestingly, Fe_3O_4 not only induced the increase of BET-surface area and pore
453 volume to improve Cr(VI) adsorption, but also stimulated the generation of more electron
454 donating carbon-centered PFRs and development of graphitic structure to enhance the
455 Cr(VI) reduction. The Fe_3O_4 and carbon-centered PFRs in the MBC accounted for 81.8%

and 18.2% of total Cr(III) generation, respectively. In addition, the initial solution pH had a significant influence on the Cr(VI) removal. Although the MBC has been systematically investigated to treat model Cr(VI)-containing water, the application of MBC for practical Cr(VI)-contaminated water treatment needs to be further studied, especially the corresponding Cr(VI) removal mechanisms.

Acknowledgements

This work was supported by the National Natural Science Foundation of China (No. 41671311), the National High Technology Research and Development (863) Program of China (No. 2012AA06A304) and Fundamental Research Funds for the Central Universities (No. 2015QN124) the Project of 356 Innovative and Interdisciplinary Teams of Huazhong University of Science and Technology (No. 0118261077), and Key Project in the National Science & Technology Pillar Program during the Twelfth Five-year Plan Period (No. 2015BAB01B04). The authors would like to thank the Analytical and Testing Center, Huazhong University of Science and Technology, China, for the kind help with sample characterization. Authors also acknowledge the support by the Brook Byers Institute for Sustainable Systems, Hightower Chair, and the Georgia Research Alliance at the Georgia Institute of Technology.

References

Bhargava, G., Gouzman, I., Chun, C.M., Ramanarayanan, T.A., Bernasek, S.L., 2007. Characterization of the "native" surface thin film on pure polycrystalline iron: A high resolution XPS and TEM study. Appl. Surf. Sci. 253, 4322–4329.

Cao, Y., Huang, J., Li, Y., Qiu, S., Liu, J., Khasanov, A., Khan, M.A., Young, D.P., Peng, F., Cao, D., Peng, X., Hong, K., Guo, Z., 2016. One-pot melamine derived nitrogen doped magnetic carbon nanoadsorbents with enhanced chromium removal. Carbon 109, 640–649.

Chu, G., Zhao, J., Chen, F., Dong, X., Zhou, D., Liang, N., Wu, M., Pan, B., Steinberg, C.E.W., 2017. Physi-chemical and sorption properties of biochars prepared from peanut shell using thermal pyrolysis and microwave irradiation. Environ. Pollut. 227, 372–379.

Cui, L., Wang, Y., Gao, L., Hu, L., Yan, L., Wei, Q., Du, B., 2015. EDTA functionalized magnetic graphene oxide for removal of Pb(II), Hg(II) and Cu(II) in water treatment: Adsorption mechanism and separation property. Chem. Eng. J. 281, 1–10.

Duan, W., Chen, G., Chen, C., Sanghvi, R., Iddya, A., Walker, S., Liu, H., Ronen, A., Jassby, D., 2017. Electrochemical removal of hexavalent chromium using electrically conducting carbon nanotube/polymer composite ultrafiltration membranes. J. Membrane Sci. 531, 160–171.

Eltouny, N.A., Ariya, P.A., 2012. Fe_3O_4 Nanoparticles and carboxymethyl cellulose: A green option for the removal of atmospheric benzene, toluene, ethylbenzene, and o-xylene (BTEX). Ind. Eng. Chem. Res. 51, 12787–12795.

Fang, G., Gao, J., Liu, C., Dionysiou, D.D., Wang, Y., Zhou, D., 2014. Key role of persistent free radicals in hydrogen peroxide activation by biochar: Implications to organic contaminant degradation. Environ. Sci. Technol. 48, 1902−1910.

Fang, G., Liu, C., Gao, J., Dionysiou, D.D., Zhou, D., 2015a. Manipulation of persistent free radicals in biochar to activate persulfate for contaminant degradation. Environ. Sci. Technol. 49, 5645−5653.

Fang, G., Zhu, C., Dionysiou, D.D., Gao, J., Zhou, D., 2015b. Mechanism of hydroxyl radical generation from biochar suspensions: Implications to diethyl phthalate degradation. Bioresource Technol. 176, 210–217.

Guo, J., Lian, J., Xu, Z., Xi, Z., Yang, J., Jefferson, W., Liu, C., Li, Z., Yue, L., 2012. Reduction of Cr(VI) by Escherichia coli BL21 in the presence of redox mediators. Bioresource Technol. 123, 713–716.

He, Y.T., Traina, S.J., 2005. Cr(VI) reduction and immobilization by magnetite under alkaline pH conditions: The role of passivation. Environ. Sci. Technol. 39, 4499–4504.

Jiang, W., Cai, Q., Xu, W., Yang, M., Cai, Y., Dionysiou, D.D., O'Shea, K.E., 2014. Cr(VI) adsorption and reduction by humic acid coated on magnetite. Environ. Sci. Technol. 48, 8078−8085.

Jin, Z., Wang, X., Sun, Y., Ai, Y., Wang, X., 2015. Adsorption of 4-n-nonylphenol and

bisphenol-A on magnetic reduced graphene oxides: A combined experimental and theoretical studies. Environ. Sci. Technol. 49, 9168−9175.
Kanari, N., Menad, N., Diot, F., Yvon, J., 2016. Thermal treatment of hydrated ferrous sulfate waste under different atmospheres, pp. 1178–1185, Albi, France.
Katz Sidney, A., Salem, H., 1993. The toxicology of chromium with respect to its chemical speciation: A review. J. Appl. Toxicol. 13, 217–224.
Li, J., Wang, Y., Song, J., Gao, Q., Zhang, J., Zhang, J., Zhai, D., Zhou, J., Liu, Q., Xu, Z.P., Qian, G., Liu, Y., 2017. Theoretical and experimental evidence for the carbon–oxygen group enhancement of NO reduction. Environ. Sci.Technol. 51, 14209–14216.
Li, Y., Zhu, S., Liu, Q., Chen, Z., Gu, J., Zhu, C., Lu, T., Zhang, D., Ma, J., 2013. N-doped porous carbon with magnetic particles formed in situ for enhanced Cr(VI) removal. Water Res. 47, 4188−4197.
Liao, P., Li, W., Jiang, Y., Wu, J., Yuan, S., Fortner, J.D., Giammar, D.E., 2017. Formation, aggregation, and deposition dynamics of NOM-iron colloids at anoxic–oxic interfaces. Environ. Sci. Technol. 51, 12235–12245.
Liu, C., Fiol, N., Villaescusa, I., Poch, J., 2016. New approach in modeling Cr(VI) sorption onto biomass from metal binary mixtures solutions. Sci. Tot. Environ. 541, 101–108.
Liu, C.H., Chuang, Y.H., Chen, T.Y., Tian, Y., Li, H., Wang, M.K., Zhang, W., 2015. Mechanism of arsenic adsorption on magnetite nanoparticles from water: Thermodynamic and spectroscopic studies. Environ. Sci. Technol. 49, 7726−7734.
Liu, Y., Wang, Y., Zhou, S., Lou, S., Yuan, L., Gao, T., Wu, X., Shi, X., Wang, K., 2012. Synthesis of high saturation magnetization superparamagnetic Fe_3O_4 hollow microspheres for swift chromium removal. ACS Appl. Mater. Inter. 4, 4913−4920.
Luo, W., Wang, B., Heron, C.G., Allen, M.J., Morre, J., Maier, C.S., Stickle, W.F., Ji, X., 2014. Pyrolysis of cellulose under ammonia leads to nitrogen-doped nanoporous carbon generated through methane formation. Nano Lett. 14, 2225−2229.
Mohan, D., Kumar, H., Sarswat, A., Alexandre-Franco, M., Pittman, C.U., 2014. Cadmium and lead remediation using magnetic oak wood and oak bark fast pyrolysis bio-chars. Chem. Eng. J. 236, 513−528.
Pan, C., Troyer, L.D., Catalano, J.G., Giammar, D.E., 2016. Dynamics of chromium(VI) removal from drinking water by iron electrocoagulation. Environ. Sci. Technol. 50, 13502–13510.
Pinakidou, F., Katsikini, M., Simeonidis, K., Kaprara, E., Paloura, E.C., Mitrakas, M., 2016. On the passivation mechanism of Fe_3O_4 nanoparticles during Cr(VI) removal from water: A XAFS study. Appl. Surf. Sci. 360, 1080–1086.
Qian, L., Zhang, W., Yan, J., Han, L., Chen, Y., Ouyang, D., Chen, M., 2017. Nanoscale zero-valent iron supported by biochars produced at different temperatures: Synthesis mechanism and effect on Cr(VI) removal. Environ. Pollut. 223, 153–160.
Qiu, B., Gu, H., Yan, X., Guo, J., Wang, Y., Sun, D., Wang, Q., Khan, M., Zhang, X., Weeks, B.L., Young, D.P., Guo, Z., Wei, S., 2014. Cellulose derived magnetic

mesoporous carbon nanocomposites with enhanced hexavalent chromium removal. J. Mater. Chem. A 2, 17454–17462.
Qiu, B., Wang, Y., Sun, D., Wang, Q., Zhang, X., Weeks, B.L., O'Connor, R., Huang, X., Wei, S., Guo, Z., 2015. Cr(VI) removal by magnetic carbon nanocomposites derived from cellulose at different carbonization temperatures. J. Mater. Chem. A 3, 9817–9825.
Rajput, S., Pittman Jr, C.U., Mohan, D., 2016. Magnetic magnetite (Fe_3O_4) nanoparticle synthesis and applications for lead (Pb^{2+}) and chromium (Cr^{6+}) removal from water. J. Colloid Interf. Sci. 468, 334−346.
Rao, A., Bankar, A., Kumar, A.R., Gosavi, S., Zinjarde, S., 2013. Removal of hexavalent chromium ions by Yarrowia lipolytica cells modified with phyto-inspired Fe^0/Fe_3O_4 nanoparticles. J. Contam. Hydrol. 146, 63–73.
Rapti, S., Pournara, A., Sarma, D., Papadas, I.T., Armatas, G.S., Tsipis, A.C., Lazarides, T., Kanatzidis, M.G., Manos, M.J., 2016. Selective capture of hexavalent chromium from an anion-exchange column of metal organic resin-alginic acid composite. Chem. Sci. 7, 2427–2436.
Ren, Y., Abbood, H.A., He, F., Peng, H., Huang, K., 2013. Magnetic EDTA-modified chitosan/SiO_2/Fe_3O_4 adsorbent: Preparation, characterization, and application in heavy metal adsorption. Chem. Eng. J. 226, 300–311.
Sun, G., Dong, B., Cao, M., Wei, B., Hu, C., 2011. Hierarchical dendrite-like magnetic materials of Fe_3O_4, γ-Fe_2O_3, and Fe with high performance of microwave absorption. Chem. Mater. 23, 1587−1593.
Veerakumar, P., Panneer Muthuselvam, I., Hung, C.-T., Lin, K.-C., Chou, F.-C., Liu, S.-B., 2016. Biomass-derived activated carbon supported Fe_3O_4 nanoparticles as recyclable catalysts for reduction of nitroarenes. ACS Sustain. Chem. Eng. 4, 6772−6782.
Wang, G., Gao, Z., Wan, G., Lin, S., Yang, P., Qin, Y., 2014. High densities of magnetic nanoparticles supported on graphene fabricated by atomic layer deposition and their use as efficient synergistic microwave absorbers. Nano Res. 7, 704−716.
Wang, S., Tang, Y., Li, K., Mo, Y., Li, H., Gu, Z., 2014. Combined performance of biochar sorption and magnetic separation processes for treatment of chromium-contained electroplating wastewater. Bioresource Technol. 174, 67–73.
Wang, T., Zhang, L., Li, C., Yang, W., Song, T., Tang, C., Meng, Y., Dai, S., Wang, H., Chai, L., Luo, J., 2015. Synthesis of core–shell magnetic Fe_3O_4@poly(m-phenylenediamine) particles for chromium reduction and adsorption. Environ. Sci. Technol. 49, 5654−5662.
Wilson, D., Langell, M.A., 2014. XPS analysis of oleylamine/oleic acid capped Fe_3O_4 nanoparticles as a function of temperature. Appl. Surf. Sci. 303, 6–13.
Yamashita, T., Hayes, P., 2008. Analysis of XPS spectra of Fe^{2+} and Fe^{3+} ions in oxide materials. Appl. Surf. Sci. 254, 2441−2449.
Yang, J., Pan, B., Li, H., Liao, S., Zhang, D., Wu, M., Xing, B., 2016. Degradation of p-

nitrophenol on biochars: Role of persistent free radicals. Environ. Sci. Technol. 50, 694–700.
Yang, J., Pignatello, J.J., Pan, B., Xing, B., 2017. Degradation of p-nitrophenol by lignin and cellulose chars: H_2O_2-mediated reaction and direct reaction with the char. Environ. Sci. Technol. 51, 8972–8980.
Yao, D., Hu, Q., Wang, D., Yang, H., Wu, C., Wang, X., Chen, H., 2016. Hydrogen production from biomass gasification using biochar as a catalyst/support. Bioresource Technol. 216, 159–164.
Yuan, P., Liu, D., Fan, M., Yang, D., Zhu, R., Ge, F., Zhu, J., He, H., 2010. Removal of hexavalent chromium [Cr(VI)] from aqueous solutions by the diatomite-supported/unsupported magnetite nanoparticles. J. Hazard. Mater. 173, 614−621.
Zhang, C., Lai, C., Zeng, G., Huang, D., Yang, C., Wang, Y., Zhou, Y., Cheng, M., 2016. Efficacy of carbonaceous nanocomposites for sorbing ionizable antibiotic sulfamethazine from aqueous solution. Water Res. 95, 103−112.
Zhang, J., Chen, L., Yin, H., Jin, S., Liu, F., Chen, H., 2017a. Mechanism study of humic acid functional groups for Cr(VI) retention: Two-dimensional FTIR and 13C CP/MAS NMR correlation spectroscopic analysis. Environ. Pollut. 225, 86–92.
Zhang, J., Chen, L., Yin, H., Jin, S., Liu, F., Chen, H., 2017b. Mechanism study of humic acid functional groups for Cr(VI) retention: Two-dimensional FTIR and ^{13}C CP/MAS NMR correlation spectroscopic analysis. Environ. Pollut. 225, 86−92.
Zhao, T.-T., Ge, W.-Z., Yue, F., Wang, Y.-X., Pedersen, C.M., Zeng, F.-G., Qiao, Y., 2016. Mechanism study of Cr(III) immobilization in the process of Cr(VI) removal by Huolinhe lignite. Fuel Process. Technol. 152, 375–380.
Zhou, L., Zhang, G., Wang, M., Wang, D., Cai, D., Wu, Z., 2018. Efficient removal of hexavalent chromium from water and soil using magnetic ceramsite coated by functionalized nano carbon spheres. Chem. Eng. J. 334, 400–409.